

Figure 1 Interaction radii for Li and Be isotopes using three different targets [1].

## Sizes and energies of exotic nuclei

### 1 Introduction

The first experiments with unstable nuclear beams were designed to measure the nuclear sizes, namely the matter distribution of protons and neutrons. For stable nuclei such experiments are best accomplished with electron beams, which probe the nuclear charge (proton) distribution. Electron scattering experiments with unstable beams can only be performed in an electron-nucleus collider. Such machines are not yet available. The easiest solution is to measure the *interaction cross section* in collisions of unstable beams with a fixed target nucleus.

The interaction cross section is defined as the cross section for the change of proton and/or neutron number in the incident nucleus. To extract the *interaction radii* of the radioactive secondary beam nuclei, one has assumed that it can be expressed as [1]

$$\sigma_I(P, T) = \pi [R_I(P) + R_I(T)]^2 \quad (1)$$

where  $R_I(P)$  and  $R_I(T)$  are the interaction radii of the projectile and the target nuclei, respectively.  $R_I(T)$  can be obtained from  $\sigma_I$  in collisions between identical nuclei, while  $R_I(P)$  can be obtained by measuring  $\sigma_I$  for different targets  $T$  [1].

The above equation assumes a separability of the projectile and target radius. This hypothesis has been tested by Tanihata and collaborators [1]. As an example, the interaction radii  $R_I$  for Li and Be isotopes have been obtained using three different targets. The results are shown in Fig. 1.

In Table 3.1 we show in the first column the interaction radii of several nuclei

obtained with this technique [1]. In the last column the root mean charge radius of some nuclei obtained by electron scattering,  $R_{\text{rms}}^e$ , are also shown. One observes that  $R_{\text{rms}}^e$  is almost constant for  $A \geq 6$ , while  $R_I$  increases with  $A$ . One can show that this difference is due to the definitions of the two radii but not due to a difference between the charge and the matter distributions. To prove it we use an eikonal calculation for the cross sections. The *rms* radius of the matter density can be determined independently of the assumed model density functions.

## 2 Reaction cross sections

The reaction cross section in high energy collisions is given by

$$\sigma_R = 2\pi \int [1 - T(b)] b db, \quad (2)$$

where

$$T(b) = \exp \left\{ -\sigma_{NN} \int_{-\infty}^{\infty} dz \int \rho_P(\mathbf{r}) \rho_T(\mathbf{R} + \mathbf{r}) d^3r \right\} \quad (3)$$

with  $\mathbf{R} = (\mathbf{b}, z)$ .  $\sigma_{NN}$  is the nucleon-nucleon cross section at the corresponding bombarding energy, and  $\rho_{P(T)}$  is the projectile (target) matter density distribution.  $T(b)$  is known as the *transparency function*.

The data compiled in Table 3.1 were obtained by measuring the cross sections for the interaction of the projectiles listed in the left part of the Table with several targets at a bombarding energy of 790 MeV/nucleon. At this energy the (free) nucleon-nucleon cross section is  $\sigma_{NN} = 40 \text{ mb}$ . Also, at these energies we can assume that the interaction cross sections and the reaction cross sections are equal (the reaction cross section includes nuclear excitations besides of fragmentation).

The simplest parametrization for the nuclear matter densities are Gaussians. Assuming

$$\rho_{P(T)}(r) = \rho_{P(T)}(0) \exp \left\{ -r^2/a_{P(T)}^2 \right\} \quad (4)$$

the integral in Eq. 3 can be performed analytically. One gets

$$T(b) = \exp \left\{ -\frac{\pi^2 \sigma_{NN} \rho_T(0) \rho_P(0) a_T^3 a_P^3}{(a_T^2 + a_P^2)} \exp \left[ -\frac{b^2}{(a_T^2 + a_P^2)} \right] \right\}. \quad (5)$$

The integral in Eq. 2 can also be done analytically by using the identity

$$\int_0^x \frac{1 - e^{-u}}{u} du = E_1(x) + \ln x + \gamma, \quad (6)$$

where

$$E_1(x) = \int_x^{\infty} \frac{e^{-u}}{u} du \quad (7)$$

is the exponential integral [3], and  $\gamma = 0.5772 \dots$  is the Euler's constant.

The final expression for  $\sigma_R$  is [4]\*

$$\sigma_R = \pi (a_p^2 + a_T^2) [E_1(x) + \ln x + \gamma] \quad (8)$$

where

$$x = \frac{\pi^2 \sigma_{NN} \rho_T(0) \rho_P(0) a_T^3 a_P^3}{(a_T^2 + a_P^2)} . \quad (9)$$

Except for the very light nuclei (as  $\alpha$ -particles and carbon nuclei) the Gaussian parametrization is not a good one. A Fermi function is more adequate in most cases. However, as observed by Karol [4] the absorption probability term  $[1 - T(b)]$  which enters in Eq. 2 is very little dependent on the lower values of  $b$  and consequently on the values of  $\rho_{P(T)}(r)$  for small  $r$ 's. Only the surface form of the density is relevant. Thus, one can fit the surface part of the densities by Gaussians and use the Eq. 8 for  $\sigma_R$  with the appropriate fitting parameters  $\rho_P(0)$ ,  $\rho_T(0)$ ,  $a_T$  and  $a_P$ . If the density distributions are described by a Fermi function

$$\rho(r) = \rho_0 \{1 + \exp[(r - R)/c]\}^{-1} \quad (10)$$

it can be shown [4] that  $[1 - T(b)]$  is well reproduced with Eq. 4 if the parameters in the Gaussian distributions are given by

$$t = (4 \ln 3) c = (4.39444\dots) c, \quad a^2 = \frac{4Rt + t^2}{k}, \quad \rho(0) = \frac{1}{2} \rho_0 e^{R^2/a^2}, \quad (11)$$

where

$$\rho_0 = \frac{3A}{4\pi R^3 [1 + (\pi^2 c^2/R^2)]}, \quad k = 4 \ln 5 = 6.43775\dots \quad (12)$$

where  $A$  is the mass number.

		$R_{\text{rms}}$			
	$R_I$	Gaussian (matter)	Harmonic osc. (matter)	(charge) <sup>a</sup>	Electron scatt. (charge)
<sup>4</sup> He	1.41 ± 0.03	1.59 ± 0.04	1.57 ± 0.04	1.57 ± 0.04	1.67 ± 0.01
<sup>6</sup> He	2.18 ± 0.02	2.52 ± 0.03	2.48 ± 0.03	2.21 ± 0.03	
<sup>8</sup> He	2.48 ± 0.03	2.55 ± 0.03	2.52 ± 0.03	2.15 ± 0.02	
<sup>6</sup> Li	2.09 ± 0.02	2.35 ± 0.03	2.32 ± 0.03	2.32 ± 0.03	2.56 ± 0.10
<sup>7</sup> Li	2.23 ± 0.02	2.35 ± 0.03	2.33 ± 0.02	2.27 ± 0.02	2.41 ± 0.10
<sup>8</sup> Li	2.36 ± 0.02	2.38 ± 0.02	2.37 ± 0.02	2.26 ± 0.02	
<sup>9</sup> Li	2.41 ± 0.02	2.32 ± 0.02	2.32 ± 0.02	2.18 ± 0.02	
<sup>11</sup> Li	3.14 ± 0.16	3.10 ± 0.17	3.12 ± 0.16	2.88 ± 0.11	
<sup>7</sup> Be	2.22 ± 0.02	2.33 ± 0.02	2.31 ± 0.02	2.36 ± 0.02	
<sup>9</sup> Be	2.45 ± 0.01	2.38 ± 0.01	2.38 ± 0.01	2.34 ± 0.01	2.52 ± 0.01
<sup>10</sup> Be	2.46 ± 0.03	2.28 ± 0.02	2.30 ± 0.02	2.24 ± 0.02	
<sup>12</sup> C	2.61 ± 0.02	2.32 ± 0.02	2.35 ± 0.02	2.35 ± 0.02	2.45 ± 0.01

\*Misprints appearing in Ref. [4] were corrected.

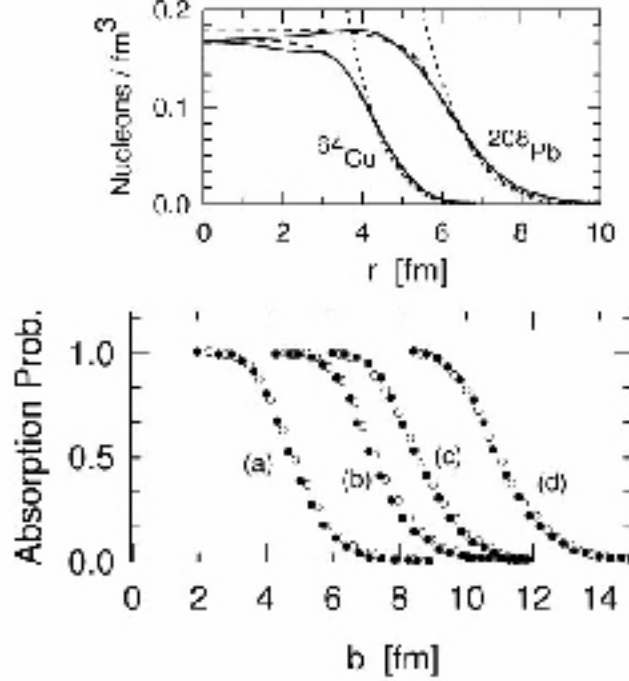


Figure 2 Upper figure: Nucleon density distribution for  $^{64}\text{Cu}$  and  $^{208}\text{Pb}$ . Solid lines represent the experimental data. Dashed lines are the Fermi distributions, and dotted lines are the Gaussian distributions which fit the surface region. Lower figure: absorption probability  $1 - T(b)$  for (a)  $^{64}\text{Cu} + ^{14}\text{N}$ ,  $^{64}\text{Cu} + ^{40}\text{Ar}$ ,  $^{208}\text{Pb} + ^{14}\text{N}$ , and  $^{208}\text{Pb} + ^{40}\text{Ar}$ . Solid circles are calculations using Fermi (or experimental) distributions, open circles are the calculations using Gaussian densities, following Karol [4].

Table 3.1. Comparison of the interaction radii and the rms radii of several light nuclei. The radii obtained in electron scattering experiments are shown in the last column. Adapted from Refs. [1, 2].

The upper part of figure 2 shows the nucleon density distributions for  $^{64}\text{Cu}$  and  $^{208}\text{Pb}$ . The solid curves are Fermi distributions with  $R = 4.34$  fm and  $t = 2.15$  fm for Cu, and  $R = 6.32$  fm and  $t = 2.73$  fm for Pb, respectively. The dotted curves correspond to the “surface normalized” Gaussian distributions (Eqs. 11, 12), which cross the Fermi distributions at the 50% and 10% central density values. In the lower part of Fig. 2 one sees the absorption probabilities  $[1 - T(b)]$  as a function of impact parameter for collisions of Cu and Pb targets with N and Ar projectiles at  $E_{\text{lab}} = 2.1$  GeV/nucleon. For this energy  $\sigma_{NN} = 35$  mb. The open circles are evaluated using the surface-normalized Gaussian distributions while the closed circles used Fermi distributions. One can see that the approximation proposed by Karol [4] works extremely well and is therefore very useful for the calculation of total reaction cross sections in high energy collisions.

For the light nuclei in Table 1.2 the Gaussian distribution gives a good de-

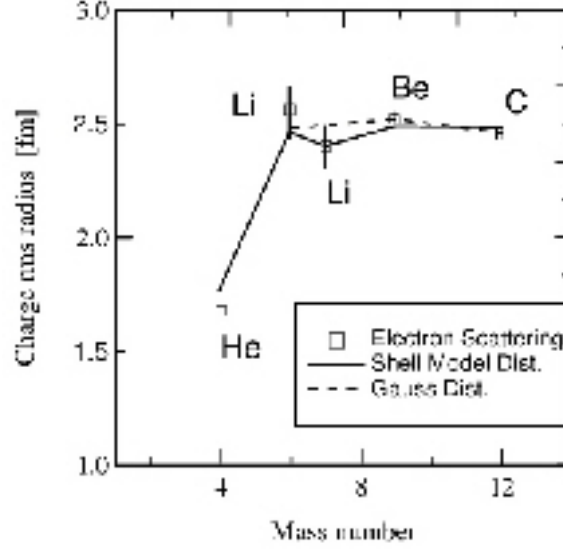


Figure 3 Comparison of calculated rms charge radii with those obtained by electron-scattering experiments with stable nuclei. The calculations using harmonic-oscillator distributions are shown by the solid line. Calculations using Gaussian distributions (which are the same for protons as for neutrons) is shown by the dashed-line.

scription of the full densities. Thus, we can use

$$\rho(r) = \frac{A}{(a\sqrt{\pi})^3} e^{-r^2/a^2} \quad (13)$$

where  $A$  is the mass number, and  $a$  is related to the root mean square radius  $R_{\text{rms}}$  by

$$a = \sqrt{\frac{2}{3}} R_{\text{rms}}. \quad (14)$$

The reaction cross sections can be calculated using the matter distributions of the target in Eq. 2, or by means of the approximation 8. The  $R_{\text{rms}}$  radii of the projectiles obtained in these calculations are listed in the second column of Table 1.2 by a comparison of  $\sigma_R$  with the experimental values of  $\sigma_I$ .

The reactions cross sections were also calculated [1] by using harmonic oscillator wavefunctions to obtain the nuclear densities (see Supplement A). The  $R_{\text{rms}}$  radii of these densities needed to reproduce the experimental values of  $\sigma_I$  are given in the 3rd and 4th column of Table 3.1. The charge distributions were obtained by folding the charge distributions of a proton with the proton density calculated with the harmonic oscillator wavefunctions,

$$\rho_p(r) = \frac{1}{r^2} \sum_{n\ell(\text{protons})} R_{n\ell}^2(r). \quad (15)$$

One finds

$$R_{\text{rms}}^C = \left[ (R_{\text{rms}}^P)^2 + (0.8)^2 \right]^{1/2} \text{ fm} \quad (16)$$

where 0.8 fm is the rms charge radius of a proton.

## Supplement A

### 2.1 Harmonic oscillator model

The radial harmonic-oscillator potential is given by

$$V(r) = \frac{1}{2} m\omega^2 r^2. \quad (17)$$

The Schrödinger equation

$$\left[ \nabla^2 + \frac{2m}{\hbar^2} (E - V(r)) \right] \psi(\mathbf{r}) = 0 \quad (18)$$

with

$$\psi_{n\ell m}(\mathbf{r}) = \frac{R_{n\ell}(r)}{r} Y_{\ell m}(\theta, \phi) \quad (19)$$

reduces to

$$\left[ \frac{d^2}{dr^2} - \frac{\ell(\ell+1)}{r^2} + \frac{2m}{\hbar^2} (E_{n\ell} - V(r)) \right] R_{n\ell}(r) = 0 \quad (20)$$

where  $n$  is the number of nodes in  $R_{n\ell}$  including the one at the origin,  $\ell$  is the angular momentum.

The solution of 20, with 17, is

$$R_{n\ell}(r) = N_{n\ell} \exp\left(-\frac{1}{2}\nu r^2\right) r^{\ell+1} \vartheta_{n\ell}(r) \quad (21)$$

where  $\nu = M\omega/\hbar$  and  $\vartheta_{n\ell}(r)$  is the Laguerre polynomial

$$\vartheta_{n\ell}(r) = L_{n+\ell-1/2}^{\ell+1/2}(\nu r^2) = \sum_{k=0}^{n-1} (-1)^k 2^k \binom{n-1}{k} \frac{(2\ell+1)!!}{(2\ell+2k+1)!!} (\nu r^2)^k.$$

From the normalization condition

$$\int_0^\infty R_{n\ell}^2(r) dr = 1 \quad (22)$$

one gets

$$N_{n\ell}^2 = \frac{2^{\ell-n+3} (2\ell+2n-1)!!}{\sqrt{\pi} (n-1)! [(2\ell+1)!!]^2} \nu^{\ell+3/2}. \quad (23)$$

The energy eigenvalue corresponding to the wavefunction  $\psi_{n\ell m}(r)$  is

$$E_{n\ell} = \hbar\omega \left( 2n + \ell - \frac{1}{2} \right) = \hbar\omega \left( \Lambda + \frac{3}{2} \right) = E_\Lambda \quad (24)$$

with

$$n = 1, 2, 3, \dots; \quad \ell = 0, 1, 2, \dots; \quad \Lambda = 2n + \ell - 2$$

For each  $\ell$ -value there are  $2(2\ell + 1)$  states with the same energy (degenerate states). The factor 2 is due to two spin states. However, the eigenvalues corresponding to the same value of  $2n + \ell$  (same value of  $\Lambda$ ) are also degenerate. Since  $2n = \Lambda - \ell + 2 = \text{even}$ , for a given value of  $\Lambda$ , the degenerate eigenstates are

$$(n, \ell) = \left( \frac{\Lambda + 2}{2}, 0 \right), \left( \frac{\Lambda}{2}, 2 \right), \dots, (2, \Lambda - 2), (1, \Lambda) \quad \text{for } \Lambda = \text{even}$$

$$(n, \ell) = \left( \frac{\Lambda + 1}{2}, 1 \right), \left( \frac{\Lambda - 1}{2}, 3 \right), \dots, (2, \Lambda - 2), (1, \Lambda) \quad \text{for } \Lambda = \text{odd}$$

so that the number of neutrons or protons with the eigenvalue  $E_\Lambda$  is (setting  $\ell = 2k$  or  $2k + 1$  according whether  $\Lambda$  is even or odd)

$$N_\Lambda = \sum_{k=0}^{\Lambda/2} 2[2(2k) + 1] \quad \text{for even } \Lambda$$

$$N_\Lambda = \sum_{k=0}^{(\Lambda-1)/2} 2[2(2k + 1) + 1] \quad \text{for odd } \Lambda. \quad (25)$$

That is

$$N_\Lambda = (\Lambda + 1)(\Lambda + 2) \quad \text{in either case,} \quad (26)$$

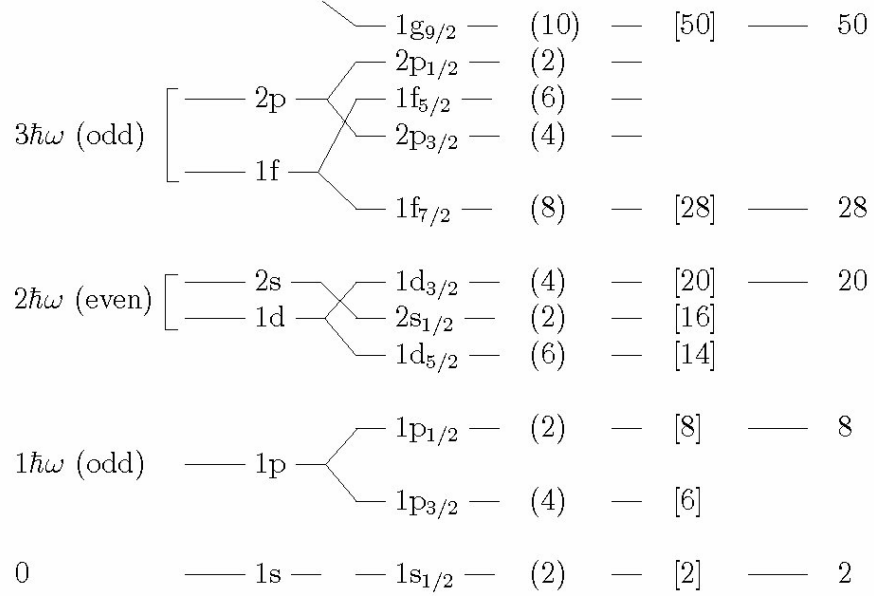
The accumulating total number of particles for all levels up to  $\Lambda$  is

$$\sum_{\Lambda} N_\Lambda = \frac{1}{3}(\Lambda + 1)(\Lambda + 2)(\Lambda + 3). \quad (27)$$

The single-particle level scheme predicted by the infinite harmonic-oscillator well is given in Table 3.2. One observes that closed shells occur at 2, 8 and 20, in agreement with experimental evidence, but predicted shell closures at higher nucleon numbers are in disagreement.

$\Lambda = 2n + \ell - 2$	$E/\hbar\omega$	Degenerate States $n\ell$ for each $\Lambda$	$N_\Lambda$	Accumulating number = $\sum_{\Lambda} N_\Lambda$
0	3/2	1s	2	2
1	5/2	1p	6	8
2	7/2	2s, 1d	12	20
3	9/2	2p, 1f	20	40
4	11/2	3s, 2d, 1g	30	70
5	13/2	3p, 2f, 1h	42	112
6	15/2	4s, 3d, 2g, 1i	56	168

Table 3.2 - Quantum numbers of the tridimensional harmonic oscillator.

Figure 4 Shell model configuration of  $A < 50$  nuclei.

To obtain the magic numbers 28, 50, 82 and 126 correctly one needs to use a potential with shape between a square-well and a harmonic oscillator. One normally uses a Woods-Saxon (Fermi) form

$$V = -V_0 \left\{ 1 + \exp \left( \frac{r - R}{a} \right) \right\}^{-1} \quad (28)$$

But this is not sufficient. One needs also to include a spin-orbit potential [5]

$$-f(r) (\mathbf{l} \cdot \mathbf{s}) \quad (29)$$

This term depresses the  $j = \ell + 1/2$  level relative to the  $j = \ell - 1/2$  one. In fact, since  $\mathbf{J} = \mathbf{l} + \mathbf{s}$ ,

$$\begin{aligned} \langle \mathbf{l} \cdot \mathbf{s} \rangle &= \frac{1}{2} \{ \langle j^2 \rangle - \langle \ell^2 \rangle - \langle s^2 \rangle \} \\ &= \frac{1}{2} [j(j+1) - \ell(\ell+1) - s(s+1)] \\ &= \begin{cases} \frac{1}{2}\ell & \text{for } j = \ell + 1/2 \\ -\frac{1}{2}(\ell+1) & \text{for } j = \ell - 1/2 \end{cases} \end{aligned} \quad (30)$$

In Fig. 4 we show the effect of the spin-orbit potential on the levels of a potential with a shape between a square-well and a harmonic oscillator. By adding the spin-orbit term the magic numbers (on the right) are reproduced.

For the light nuclei the radial density distribution

$$\rho(r) = \frac{1}{r^2} \sum_{[n\ell]} R_{\ell n}^2(r) \quad (31)$$

maybe calculated by using the harmonic oscillator wavefunctions 21.

For a harmonic-oscillator potential the expectation value of the kinetic energy in any state is equal to the expectation value of the potential energy. Thus the total single-particle energies in a nucleus of mass number  $A$  are

$$E = m\omega^2 A \langle r^2 \rangle. \quad (32)$$

Estimating  $\langle r^2 \rangle$  by the relation

$$\langle r^2 \rangle \cong \frac{3}{5} R^2 \quad (33)$$

with  $R \cong 1.2 A^{1/3}$  fm, assuming that  $N = Z$  and that all states up to energy  $E_{\Lambda_0}$  are occupied, we obtain

$$\begin{aligned} A &= \sum_{\Lambda=0}^{\Lambda_0} 2N_{\Lambda} = \frac{2}{3}(\Lambda_0 + 1)(\Lambda_0 + 2)(\Lambda_0 + 3) \\ &\cong \frac{2}{3}(\Lambda_0 + 2)^3 + \text{terms of order } (\Lambda_0) \end{aligned} \quad (34)$$

and

$$\frac{E}{\hbar\omega} = \sum_{\Lambda=0}^{\Lambda_0} 2N_{\Lambda} \left( \Lambda + \frac{3}{2} \right) \cong \frac{1}{2}(\Lambda_0 + 2)^4 - \frac{1}{3}(\Lambda_0 + 2)^3 + \dots \quad (35)$$

Eliminating  $(\Lambda_0 + 2)$  from the above equations and retaining terms of the highest powers of  $(\Lambda_0 + 2)$ , we obtain

$$\frac{E}{\hbar\omega} \cong \frac{1}{2} \left( \frac{3}{2} A \right)^{4/3}. \quad (36)$$

Or, using 32 and 33,

$$\hbar\omega \cong 41 A^{-1/3} \text{ MeV}. \quad (37)$$

The giant dipole resonances in nuclei are excitations with  $\Delta\ell = \pm 1$  do in fact vary with the nuclear mass as  $A^{-1/3}$  and are a good example of application of 37.

### 3 Halo nuclei

In order to show that the rms radii obtained by a comparison of reaction cross section calculations with the experimentally determined  $\sigma_I$  are equal, Fig. 3 shows the calculated rms charge radii and those obtained by electron-scattering experiments for stable nuclei. Even the difference between the radii of  ${}^6\text{Li}$  and  ${}^7\text{Li}$  because of the occupation-number difference between protons and neutrons is reproduced by the harmonic-oscillator distribution (solid line). The rms radii obtained with Gaussian distributions (which are the same for protons as for neutrons) is shown by the dashed-line.

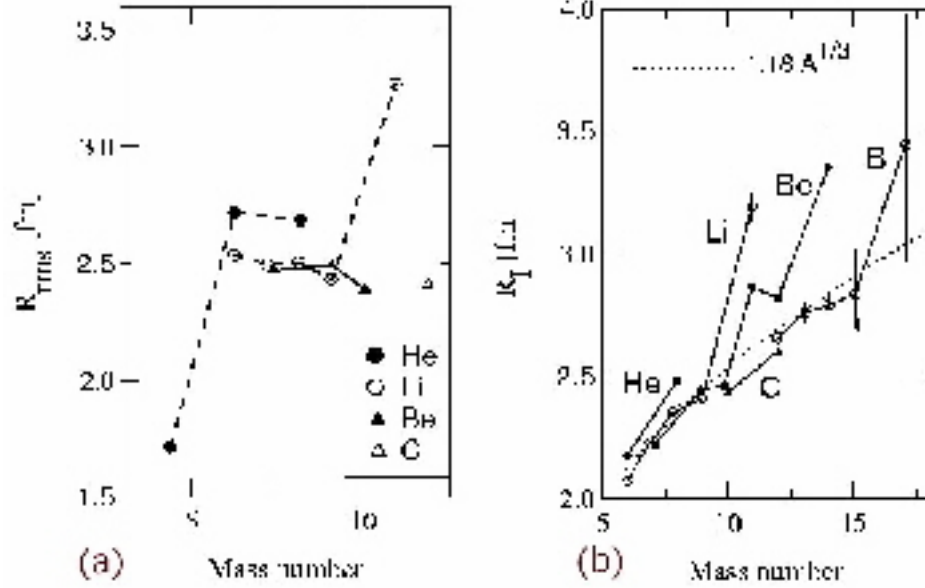


Figure 5 (a) Rms radii for the neutron-rich isotopes He, Li, Be, and C. (b) The matter density radii of several light nuclei compared to the trend  $R \sim 1.18 A^{1/3}$  fm (dashed line) for normal nuclei. The solid lines are guide to the eyes.

The calculations also show that  $R_I$  represents the radius where the matter density is about  $0.05 \text{ fm}^{-3}$  for  $A \geq 6$  nuclei. Now we can understand why the rms radii and  $R_I$  behave differently with  $A$ . While the rms radii stay constant, the absolute density increases with  $A$ . Therefore  $R_I$ , which represents constant density, increases with  $A$ . These interesting results are presented in figure 5(a) where the rms radii of He, Li, Be, and C isotopes are shown [7]. The curves are guides to the eyes.

We observe a great increase in the rms radii for the neutron-rich isotopes  ${}^6\text{He}$ ,  ${}^8\text{He}$  and  ${}^{11}\text{Li}$ . Thus, the addition of the neutrons to  ${}^4\text{He}$  and  ${}^9\text{Li}$  nuclei increase their radii considerably. This might be understood in terms of the binding energy of the outer nucleons. The large matter radii of these nuclei have lead the experimentalists to call them by “*halo nuclei*”. The binding energy of the last two neutrons in  ${}^{11}\text{Li}$  is equal to  $315 \pm 50 \text{ keV}$  [6]. In  ${}^6\text{He}$  it is  $0.97 \text{ MeV}$ . These are very small values and should be compared with  $S_n = 6 - 8 \text{ MeV}$  which is the average binding of nucleons in stable nuclei.

The wavefunction of a loosely-bound nucleon (as in the case of the deuteron) extends far beyond the nuclear potential. For large distances the wavefunction behaves as an Yukawa function,

$$R(r)/r \sim \frac{e^{-\eta r}}{r} \quad (38)$$

where  $(\hbar\eta)^2 = 2mB$ , with  $B$  equal to the binding energy and  $m$  the nucleon mass. Thus, the smaller the value of  $B$  is, the more the wavefunction extends to larger  $r$ 's.

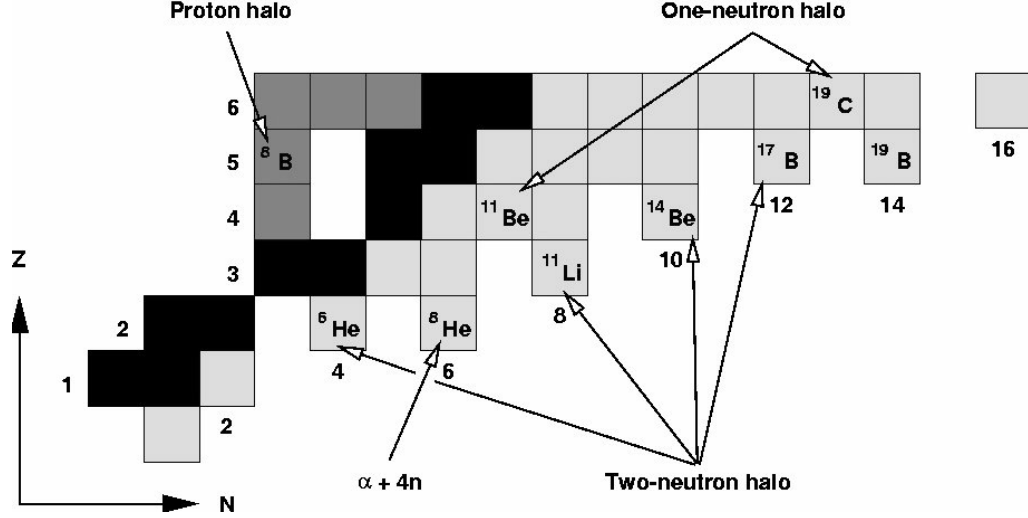


Figure 6 Nuclear chart showing the halo nuclei (by Haik Simon).

Thus the “halo” in an exotic unstable nuclei, like  $^{11}\text{Li}$ , is a simple manifestation of the weak binding energy of the last nucleons. What is not as trivial is to know why  $^6\text{He}$  and  $^{11}\text{Li}$  are bound while  $^5\text{He}$  and  $^{10}\text{Li}$  are not. We will continue this discussion later.

Abnormally large radii were also found for other light neutron-rich nuclei [7] as shown in figure 5(b).

The matter density radii of these nuclei do not follow the commonly observed trend  $R \sim 1.18 A^{1/3}$  fm of normal nuclei. Thus the halo seems to be a common feature of loosely-bound neutron-rich nuclei. In Table 3.3 we list the spin, parities and mass number of some light neutron-rich nuclei. The separation energy of one neutron ( $S_n$ ) and of two neutrons ( $S_{2n}$ ) are also shown. One observes that the two-neutron separation energies of  $^{11}\text{Li}$ ,  $^{14}\text{Be}$  and  $^{17}\text{B}$  are very small and are responsible for large matter radii of these nuclei, as seen in figure 5(b). A nuclear chart with the halo nuclei is shown in Figure 6.

## 4 Microscopic calculations of nuclear densities

---

### Supplement B

---

#### 4.1 Hartree-Fock theory

Let us consider a system of particles with a central (mean-field) potential,  $U_0$ , and a two-body (particle-particle) potential,  $v$ , as, e.g., the atomic electron system

$$H = \sum_i^A [T_i + U_0(\mathbf{r}_i)] + \frac{1}{2} \sum_{ij} v(\mathbf{r}_i, \mathbf{r}_j) \quad (39)$$

where the factor 1/2 prevents double-counting of the two-body interaction energy (see Fig. 7(a)).

Neglecting  $v(\mathbf{r}_i, \mathbf{r}_j)$ :

$$\left\{ -\frac{\hbar^2}{2m} \nabla^2 + U_0(\mathbf{r}) \right\} \psi_i(\mathbf{r}) = \epsilon_i \psi_i(\mathbf{r}). \quad (40)$$

If antisymmetrization is neglected, the total wavefunction is

$$\phi(1, 2, \dots, A) = \psi_1(1)\psi_2(2) \dots \psi_A(A) \quad (41)$$

The average interaction felt by particle  $i$  due to all other particles is

$$U_1(\mathbf{r}_i) = \sum_{j \neq i}^A \int d^3r_j |\psi_j(\mathbf{r}_j)|^2 v(\mathbf{r}_i, \mathbf{r}_j). \quad (42)$$

Now we add this potential to Eq. 40 and we obtain a new wave equation:

$$\left\{ -\frac{\hbar^2}{2m} \nabla^2 + U_0(\mathbf{r}) + U_1(\mathbf{r}) \right\} \psi_i(\mathbf{r}) = \epsilon_i \psi_i(\mathbf{r}) \quad (43)$$

The *Hartree* method is now clear: one begins with the shell-model Hamiltonian 40 and constructs the total wavefunction 41. From this wavefunction one calculates the average two-body interaction 42. One then solves the new wave equation 43. This sequence<sup>†</sup> is repeated (a process called *iteration*) until a stable solution is found. In general, only a few iterations are needed if  $|U_0(\mathbf{r})| \gg |U_1(\mathbf{r})|$ .

The *Hartree-Fock* method is easily derived from a variational method. The total wavefunction is now antisymmetrized

$$\phi(1, 2, \dots, A) = \mathcal{A} \psi_1(1)\psi_2(2) \dots \psi_A(A) \quad (44)$$

where

$$\mathcal{A} \psi_1(1)\psi_2(2) \dots \psi_A(A) = \frac{1}{\sqrt{A!}} \begin{vmatrix} \psi_1(1)\psi_2(1) & \dots & \psi_A(1) \\ \psi_1(2)\psi_2(2) & \dots & \psi_A(2) \\ \vdots & & \vdots \\ \psi_1(A)\psi_2(A) & \dots & \psi_A(A) \end{vmatrix} \quad (45)$$

is a Slater-determinant.

For a small variation  $\delta\phi$ , the energy expectation should be stationary. Thus,

$$\delta \langle \phi | H | \phi \rangle = \langle \delta\phi | H | \phi \rangle = 0. \quad (46)$$

The variation of  $\delta\phi$  should preserve the norm of the wavefunctions:

$$\int |\psi_i(\mathbf{r})|^2 d^3r = 1. \quad (47)$$

---

<sup>†</sup>41 → 42 → 43

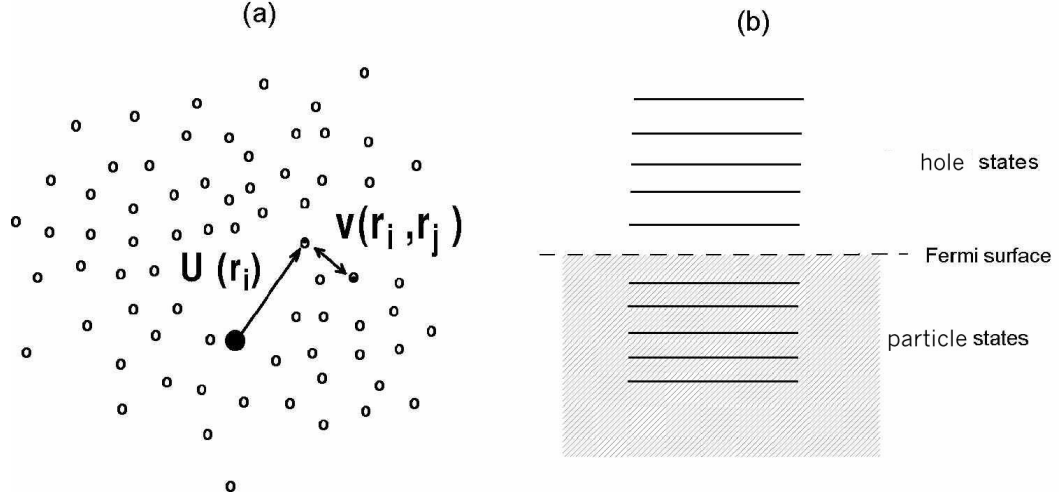


Figure 7 (a) Particles,  $i$  and  $j$ , interacting with a mean field  $U_0(\mathbf{r})$  and among themselves with an interaction  $v(\mathbf{r}_i, \mathbf{r}_j)$ . (b) Labelling of states used in Hartree-Fock calculations.

Now we solve the many-body Hamiltonian with two-body forces only (e.g., the nuclear Hamiltonian)

$$H = \sum_i^A T_i + \frac{1}{2} \sum_{ij}^A v(\mathbf{r}_i, \mathbf{r}_j) \quad (48)$$

where  $T_i = -(\hbar^2/2m) \nabla_i^2$ .

The expectation value with the wavefunction 44 is

$$\begin{aligned} \langle \phi | H | \phi \rangle &= -\frac{\hbar^2}{2m} \sum_i^A \int \psi_i^*(\mathbf{r}) \nabla^2 \psi_i(\mathbf{r}) d^3r \\ &+ \frac{1}{2} \sum_{ij}^A \iint \psi_i^*(\mathbf{r}) \psi_j^*(\mathbf{r}') v(\mathbf{r}, \mathbf{r}') \psi_i(\mathbf{r}) \psi_j(\mathbf{r}') d^3r d^3r' \\ &- \frac{1}{2} \sum_{ij}^A \iint \psi_i^*(\mathbf{r}) \psi_j^*(\mathbf{r}') v(\mathbf{r}, \mathbf{r}') \psi_i(\mathbf{r}') \psi_j(\mathbf{r}) d^3r d^3r'. \end{aligned} \quad (49)$$

The last term is a consequence of antisymmetrization. Applying the variation on  $\psi_i(\mathbf{r})$  we

obtain

$$\begin{aligned}
-\frac{\hbar^2}{2m}\nabla^2\psi_i(\mathbf{r}) &+ \sum_j^A \int d^3r' \psi_j^*(\mathbf{r}')v(\mathbf{r},\mathbf{r}')\psi_j(\mathbf{r}')\psi_i(\mathbf{r}) \\
&- \sum_j^A \int d^3r' \psi_j^*(\mathbf{r}')v(\mathbf{r},\mathbf{r}')\psi_j(\mathbf{r})\psi_i(\mathbf{r}') \\
&= \epsilon_i\psi_i(\mathbf{r})
\end{aligned} \tag{50}$$

where  $\epsilon_i$  is seen as a Lagrange multiplier that enforces the constraint 47. It has the significance of a single particle energy.

We can rewrite 50 as

$$-\frac{\hbar^2}{2m}\nabla^2\psi_i(\mathbf{r}) + \int d^3r' U(\mathbf{r},\mathbf{r}')\psi_i(\mathbf{r}') = \epsilon_i\psi_i(\mathbf{r}) \tag{51}$$

where  $U(\mathbf{r},\mathbf{r}')$  is the self-consistent field

$$U(\mathbf{r},\mathbf{r}') = \delta(\mathbf{r}-\mathbf{r}') \sum_j^A \int d^3r'' v(\mathbf{r},\mathbf{r}'')\psi_j(\mathbf{r}'')\psi_j^*(\mathbf{r}') - \sum_j^A v(\mathbf{r},\mathbf{r}')\psi_j(\mathbf{r})\psi_j^*(\mathbf{r}'). \tag{52}$$

The first term is the direct term (Hartree field). The second is called the exchange interaction and is *non-local*. This non-locality is closely related to the range of the two-body interaction. If we use a  $\delta$ -force, then the Fock (or exchange) term is also local.

In constructing the HF (Hartree-Fock) determinant one naturally selects the  $A$  lowest energy wavefunctions. Thus the HF state corresponds to a Fermi sea of particles with a sharp Fermi surface.

As in the Hartree method, one guesses a initial  $U^{(0)}$ , solves 51, finds  $\psi_i$ , calculates 52, finds new  $\psi_i$ 's, etc, until the desired accuracy is achieved.

#### 4.2 The Skyrme interaction

The most popular effective interaction used in Hartree-Fock calculations is the Skyrme interaction. It is based on the fact that a finite range interaction can be simulated by a momentum dependence. This can be shown by transforming an interaction  $V(\mathbf{r})$ , where  $\mathbf{r} = \mathbf{r}_1 - \mathbf{r}_2$ , into momentum space, i.e.,

$$\langle \mathbf{p} | v | \mathbf{p}' \rangle = \frac{1}{(2\pi\hbar)^3} \int e^{-i(\mathbf{p}-\mathbf{p}')\cdot\mathbf{r}/\hbar} v(\mathbf{r}) d^3r. \tag{53}$$

This integral gives a constant if  $v(\mathbf{r}) = \delta(\mathbf{r})$ . A finite range  $v(\mathbf{r})$  will represent a  $\mathbf{p}$ -dependence in momentum space.

The simplest form that one may find for  $\langle \mathbf{p} | v | \mathbf{p}' \rangle$  which is rotationally invariant, is

$$(2\pi\hbar)^3 \langle \mathbf{p} | v | \mathbf{p}' \rangle = v_0 + v_1 \mathbf{p}^{\prime 2} + v_1 \mathbf{p}^2 + v_2 \mathbf{p} \cdot \mathbf{p}' \tag{54}$$

which in coordinate space is related to the momentum dependent operator

$$v(\mathbf{r}) = v_0 \delta(\mathbf{r}) + v_1 [\widehat{\mathbf{p}}^2 \delta(\mathbf{r}) + \delta(\mathbf{r}) \widehat{\mathbf{p}}^2] + v_2 \widehat{\mathbf{p}} \cdot \delta(\mathbf{r}) \widehat{\mathbf{p}}. \quad (55)$$

The Skyrme interaction is based on this property and is an effective interaction with a three-body term [8, 9]

$$v = \sum_{i < j} v(i, j) + \sum_{i < j < k} v(i, j, k). \quad (56)$$

For  $v(i, j)$  one uses the form 55 with

$$\begin{aligned} v(1, 2) &= t_0 (1 + x_0 P^\sigma) \delta(\mathbf{r}_1 - \mathbf{r}_2) \\ &+ \frac{1}{2} t_1 [\delta(\mathbf{r}_1 - \mathbf{r}_2) \widehat{\mathbf{k}}^2 + \widehat{\mathbf{k}}^2 \delta(\mathbf{r}_1 - \mathbf{r}_2)] \\ &+ t_2 \widehat{\mathbf{k}} \delta(\mathbf{r}_1 - \mathbf{r}_2) \widehat{\mathbf{k}} \\ &+ i W_0 [\boldsymbol{\sigma}^{(1)} + \boldsymbol{\sigma}^{(2)}] [\widehat{\mathbf{k}} \times \delta(\mathbf{r}_1 - \mathbf{r}_2) \widehat{\mathbf{k}}] \end{aligned} \quad (57)$$

where

$$\begin{aligned} \widehat{\mathbf{k}} &= \frac{1}{\hbar} \widehat{\mathbf{p}} = \frac{1}{2i} (\nabla_1 - \nabla_2) \\ P^\sigma &= \frac{1}{2} [1 + \boldsymbol{\sigma}^{(1)} \cdot \boldsymbol{\sigma}^{(2)}]. \end{aligned} \quad (58)$$

$\boldsymbol{\sigma}$  the Dirac matrices which act on the spin part of the wavefunctions. The three-body part of the Skyrme interaction is also taken as a zero-range (delta function) force,

$$v(1, 2, 3) = t_3 \delta(\mathbf{r}_1 - \mathbf{r}_2) \delta(\mathbf{r}_2 - \mathbf{r}_3). \quad (59)$$

The constants  $t_0, t_1, t_2, t_3, x_0$  and  $W_0$  are manipulated so as to adjust the experimental binding energies and radii. There are several set of parameters often called Skyrme I, II, etc. For example, the Skyrme III interaction uses

$$\begin{aligned} t_0 &= -1128.75 \text{ MeV fm}^3, & t_1 &= 395 \text{ MeV fm}^5, \\ t_2 &= -95 \text{ MeV fm}^5, & t_3 &= 1.4 \times 10^4 \text{ MeV fm}^6, \\ W_0 &= 120 \text{ MeV fm}^5, & x_0 &= 0.45. \end{aligned} \quad (60)$$

The parameter  $t_0$  describes a pure  $\delta$ -force with a spin-exchange;  $t_1$  and  $t_2$  simulate an effective range, as in Eq. 55. The fourth term in Eq. 57 represents a two-body spin-orbit interaction. It can be obtained from a normal spin-orbit term in the short range limit.

To implement numerically a Hartree-Fock calculation with the Skyrme potential a little more algebra is necessary. In a long, but straightforward calculation, it can be shown [10] that the HF-equation in coordinate space becomes

$$\left\{ -\nabla \frac{\hbar^2}{2m^*(\mathbf{r})} \nabla + U(\mathbf{r}) + \mathbf{W} \cdot \frac{1}{i} (\nabla \times \boldsymbol{\sigma}) \right\} \psi_i(\mathbf{r}) = \epsilon_i \psi_i(\mathbf{r}) \quad (61)$$

where

$$m^*(\mathbf{r}) = m \left[ 1 + \frac{2m}{\hbar^2} \frac{1}{16} (3t_1 + 5t_2) \rho \right]^{-1} \quad (62)$$

$$\begin{aligned} U(\mathbf{r}) = & \frac{3}{4} t_0 \rho + \frac{3}{16} t_3 \rho^2 + \frac{1}{16} (3t_1 + 5t_2) \tau \\ & + \frac{1}{32} (5t_2 - 9t_1) \nabla^2 \rho - \frac{3}{4} W_0 \nabla \cdot \mathbf{J} \end{aligned} \quad (63)$$

and

$$\mathbf{W}(\mathbf{r}) = \frac{3}{4} W_0 \nabla \rho. \quad (64)$$

In the Equations above

$$\rho(\mathbf{r}) = \sum_{i,s,t} |\psi_i(\mathbf{r}, s, t)|^2 \quad (65)$$

is the nucleon density,

$$\tau(\mathbf{r}) = \sum_{i,s,t} |\nabla \psi_i(\mathbf{r}, s, t)|^2 \quad (66)$$

is the kinetic energy density, and

$$\mathbf{J}(\mathbf{r}) = -i \sum_{j,t,s,s'} \psi_j^*(\mathbf{r}, s, t) [\nabla \psi_j(\mathbf{r}, s', t) \times \boldsymbol{\sigma}_{ss'}] \quad (67)$$

is the “spin-orbit density”.  $s$  and  $t$  denote the spin and isospin quantum numbers, respectively.

We observe that  $U(\mathbf{r})$  is local and 61 is a pure differential equation. The non-locality appears only in the  $\mathbf{r}$ -dependence of  $m^*(\mathbf{r})$ , the effective nucleon mass. For a spherical symmetry 61 reduces to a one-dimensional differential equation of second order in the radial coordinate  $r$ . Then the spin-orbit term in 63 becomes

$$\frac{3}{2} W_0 \left( \frac{1}{r} \frac{\partial}{\partial r} \rho \right) \mathbf{1} \cdot \mathbf{s} \quad (68)$$

For those who do not want to write a HF-program, there are many programs of public access. For example, a very elaborate one is described in the book “Computational Nuclear Physics” [11].

---

## Supplement C

---

### 4.3 Relativistic mean field theory

It is well known from classical mechanics (see, e.g., [12]) that the dynamics of a system of particles is well defined if a Lagrangian

$$L(q_i, \dot{q}_i, t) = T - V \quad (69)$$

is given. Then, with help of the *Euler-Lagrange equations*

$$\frac{d}{dt} \left( \frac{\partial L}{\partial \dot{q}_j} \right) - \frac{\partial L}{\partial q_j} = 0 \quad (70)$$

one obtains the Newtonian equations of motion for the particle coordinates  $q_j$ . This can also be generalized in relativistic mechanics [12]. In fact the generalization can be further extended to continuous systems and to fields, the concept of a Lagrangian density  $\mathcal{L}$  is needed, so that

$$L = \int \mathcal{L} d^3r \quad (71)$$

It can be shown [12] that if the amplitude of the field is given by  $\phi(\mathbf{r}, t)$ , the Euler-Lagrange equations of motion for this field are

$$\frac{d}{dt} \left( \frac{\partial \mathcal{L}}{\partial (d\phi/dt)} \right) + \sum_{i=1}^3 \frac{d}{dx_i} \left( \frac{\partial \mathcal{L}}{\partial (d\phi/dx_i)} \right) - \frac{\partial \mathcal{L}}{\partial \phi} = 0 \quad (72)$$

where  $\mathbf{r} \equiv (x_1, x_2, x_3)$  and

$$\mathcal{L} = \mathcal{L} \left( \phi, \frac{d\phi}{dx_i}, \frac{d\phi}{dt}, x_i, t \right). \quad (73)$$

If the Lagrangian density is a function of many fields  $\phi_j$ , there will be an Euler-Lagrangian equation for each field.

As examples we quote

(a)

$$\mathcal{L} = \dot{\phi}\dot{\phi}^* - c^2 \nabla\phi \cdot \nabla\phi^* - \mu_0^2 c^2 \phi\phi^*. \quad (74)$$

We leave as an exercise to show that using the Euler-Lagrange equations 72 leads to

$$\nabla^2\phi - \frac{1}{c^2} \frac{d^2\phi}{dt^2} - \mu_0^2\phi = 0 \quad (75)$$

which is the well-known *Klein-Gordon* equation. This is a relativistic analog of the Schrödinger equation for a charged zero-spin particle of rest mass  $\mu_0$  (e.g., the pion).

(b)

$$\mathcal{L} = -\frac{1}{8\pi} \frac{dA_\mu}{dx_\nu} \frac{dA_\mu}{dx_\nu} - \frac{e}{c} \psi^\dagger \gamma_\mu A_\mu \psi + i\psi^\dagger \gamma_\mu \frac{\partial\psi}{\partial\mu} + m\psi^\dagger\psi \quad (76)$$

where  $A_\mu$  is the electromagnetic four-vector potential  $A_\mu = (\mathbf{A}, i\phi_0)$ . The above Lagrangian density describes the dynamics of a Dirac particle in an electromagnetic field. The

particle field consists of four complex scalar quantities appearing in two arrays,  $\psi$  and  $\psi^\dagger \cdot \psi$  can be considered as a four-element column matrix and  $\psi^\dagger$  as the adjoint matrix  $\left(M_{ij}^\dagger = M_{ji}^*\right)$ . Matrix multiplication and summation convention  $V_\mu W_\mu = \mathbf{V} \cdot \mathbf{W} + V_4 W_4$  is assumed in Eq. 76.

The matrices  $\gamma_i$  are generalization of the Dirac matrices,  $\gamma_4 = \beta$ ,  $\gamma = i\alpha\beta$ , i.e.,

$$\gamma_i = \begin{pmatrix} 0 & \sigma_i \\ -\sigma_i & 0 \end{pmatrix}, \quad \gamma_4 = \begin{pmatrix} 1 & 0 \\ 0 & -1 \end{pmatrix} \quad (77)$$

where  $\sigma_i$ , ( $i = 1, 2, 3$ ), are the usual Dirac matrices

$$\sigma_1 = \begin{pmatrix} 0 & 1 \\ 1 & 0 \end{pmatrix}, \quad \sigma_2 = \begin{pmatrix} 0 & -i \\ i & 0 \end{pmatrix}, \quad \sigma_3 = \begin{pmatrix} 1 & 0 \\ 0 & -1 \end{pmatrix} \quad (78)$$

using the Euler-Lagrange equations. for the field  $\psi^\dagger$  one can show that [12] ( $x_\mu = (\mathbf{r}, ict)$ );

$$\gamma_\mu \left[ i \frac{d}{dx_\mu} - \frac{e}{c} A_\mu \right] \psi + m\psi = 0 \quad (79)$$

This is the *Dirac equation* for a charged particle of charge  $e$  and mass  $m$  interacting with an electromagnetic field.

The relativistic mean field theory for the nuclear dynamics is based on a Lagrangian density that ascribes to each nucleon a Dirac field (or spinor)  $\psi_i$  which interacts with meson fields, i.e., the nucleon-nucleon interaction is assumed to arise from the exchange of mesons.

The most common Lagrangian used is given by (for a review of this theory, see [13])

$$\begin{aligned} \mathcal{L} = & \bar{\psi} (i\gamma_\mu \partial_\mu - m) \psi + \frac{1}{2} \partial_\mu \sigma \partial_\mu \sigma - U(\sigma) - \frac{1}{4} \Omega_{\mu\nu} \Omega_{\mu\nu} \\ & + \frac{1}{2} m_\omega^2 \omega_\mu \omega_\mu - \frac{1}{4} \mathbf{R}_{\mu\nu} \mathbf{R}_{\mu\nu} + \frac{1}{2} m_\rho^2 \boldsymbol{\rho}_\mu \boldsymbol{\rho}_\mu - \frac{1}{4} F_{\mu\nu} F_{\mu\nu} \\ & - g_\sigma \bar{\psi} \sigma \psi - g_\omega \bar{\psi} \gamma_\mu \omega_\mu \psi - g_\rho \bar{\psi} \gamma_\mu \boldsymbol{\rho}_\mu \boldsymbol{\tau} \psi - e \bar{\psi} \gamma_\mu A_\mu \psi \end{aligned} \quad (80)$$

where

$$\bar{\psi} = \psi^\dagger \gamma_4 \quad (81)$$

$\sigma$  is the isoscalar-scalar ( $T = 0$ ,  $S = 0$ )  $\sigma$ -meson field;

$$\Omega_{\mu\nu} = \partial_\mu \omega_\nu - \partial_\nu \omega_\mu, \quad (82)$$

in terms of the isoscalar-vector ( $T = 0$ ,  $S = 1$ )  $\omega$ -meson field,  $\omega_\mu$ ;

$$\mathbf{R}_{\mu\nu} = \partial_\mu \boldsymbol{\rho}_\nu - \partial_\nu \boldsymbol{\rho}_\mu - g_\rho (\boldsymbol{\rho}_\mu \times \boldsymbol{\rho}_\nu) \quad (83)$$

in terms of the isovector-vector ( $T = 1$ ,  $S = 1$ )  $\rho$ -meson field,  $\boldsymbol{\rho}_\mu$ ;

$$F_{\mu\nu} = \frac{\partial A_\nu}{\partial x_\mu} - \frac{\partial A_\mu}{\partial x_\nu} \quad (84)$$

is the familiar expression for the electromagnetic fields tensor;  $m$  is the nucleon mass;  $m_\sigma$ ,  $m_\omega$ , and  $m_\rho$  are the masses of the  $\sigma$ -meson, the  $\omega$ -meson, and the  $\rho$ -meson, respectively, and are the corresponding coupling constants  $g_\rho$ ,  $g_\rho$ ,  $g_\omega$ .

The  $\sigma$ -meson moves in a potential with self-interacting non-linear cubic ( $\sigma^3$ ) and quartic ( $\sigma^4$ ) terms with strength parameters  $g_2$  and  $g_3$ , respectively:

$$U(\sigma) = \frac{1}{2} m_\sigma^2 \sigma^2 + \frac{g_2}{3} \sigma^3 + \frac{g_3}{4} \sigma^4 \quad (85)$$

The Euler-Lagrange equations lead to the Dirac equation for the nucleons

$$\{-i\boldsymbol{\alpha} \cdot \boldsymbol{\nabla} + V(\mathbf{r}) + \beta(m + S(\mathbf{r}))\} \psi_i = \epsilon_i \psi_i \quad (86)$$

where  $V$  is a repulsive vector potential

$$V(\mathbf{r}) = g_\omega \omega_0(\mathbf{r}) + g_\rho \tau_3 \rho_0(\mathbf{r}) + e \frac{1 + \tau_3}{2} A_0(\mathbf{r}). \quad (87)$$

$\tau_3$  is the 3rd component of the isospin operator:  $t_3 \chi_p = -\frac{1}{2} \chi_p$ ,  $t_3 \chi_n = \frac{1}{2} \chi_n$ , where  $\chi_p$ , and  $\chi_n$  are the proton and the neutron isospin wave function, respectively.  $S$  is the attractive scalar potential

$$S(\mathbf{r}) = g_\sigma \sigma(\mathbf{r}) \quad (88)$$

contributing to the effective Dirac mass

$$m^*(\mathbf{r}) = m + S(\mathbf{r}) \quad (89)$$

The equations for the mesonic fields are also obtained from the Euler-Lagrangian equations, leading to the Klein-Gordon equations with source terms involving the baryon densities:

$$\begin{aligned} \{-\Delta + m_\sigma^2\} \sigma(\mathbf{r}) &= -g_\sigma \rho_s(\mathbf{r}) - g_2 \sigma^2(\mathbf{r}) - g_3 \sigma^3(\mathbf{r}) \\ \{-\Delta + m_\omega^2\} \omega_0(\mathbf{r}) &= g_\omega \rho_v(\mathbf{r}) \\ \{-\Delta + m_\rho^2\} \rho_0(\mathbf{r}) &= g_\rho \rho_3(\mathbf{r}) \\ -\Delta A_0(\mathbf{r}) &= e \rho_c(\mathbf{r}) \end{aligned} \quad (90)$$

The corresponding source terms are

$$\begin{aligned} \rho_s &= \sum_{i=1}^A \bar{\psi}_i \psi_i \\ \rho_v &= \sum_{i=1}^A \psi_i^\dagger \psi_i \\ \rho_3 &= \sum_{p=1}^Z \psi_p^\dagger \psi_p - \sum_{n=1}^N \psi_n^\dagger \psi_n \\ \rho_c &= \sum_{p=1}^Z \psi_p^\dagger \psi_p \end{aligned} \quad (91)$$

These set of equations known as RMF (Relativistic Mean Field) equations are solved self-consistently by iteration, as in the usual H-F procedure.

A typical set of parameters are

$$\begin{aligned}
 M_\sigma &= 504.89 & g_\sigma &= 9.111 \\
 M_\omega &= 780 & g_2 &= -2.304 \text{ fm}^{-1} \\
 M_\rho &= 763 & g_3 &= 13.783 \\
 & & g_\omega &= 11.493 \\
 & & g_f &= 5.507
 \end{aligned} \tag{92}$$

where the masses are in MeV.

The Lagrangian density 80 is based on the hypothesis that the one-pion-exchange potential contribution to the bulk properties of nuclear matter largely averages to zero [13]. A numerical implementation of a RMF is given in Ref. [11]. These set of equations known as RMF equations are solved self-consistently by iteration, as in the usual H-F procedure (see Supplement B).

---

## 5 Nuclear density calculations

In order to explain the spin, parities, separation energies and size of exotic nuclei consistently a microscopic calculation is needed. One possibility is to resort to a Hartree-Fock calculation (see Supplement B). Unfortunately, the H-F theory cannot provide the predictions for the separation energies within the required accuracy of hundred keV [14].

A fully microscopic consistent solution of this problem seems to be very difficult [17, 18]. However a simple and tractable method was suggested in Ref. [19]. The idea is the following. The H-F equation for the Skyrme interaction can be written as (see Supplement B).

$$\left[ -\nabla \frac{\hbar^2}{2m^*(r)} \nabla + V(\mathbf{r}) \right] \psi_i(\mathbf{r}) = \epsilon_i \psi_i(\mathbf{r}) \tag{93}$$

where  $m^*(\mathbf{r})$  is the effective mass. The potential  $V(\mathbf{r})$  has a central, a spin-orbit and a Coulomb term

$$V(\mathbf{r}) = V_{\text{central}} + V_{\text{spin-orbit}} + V_{\text{Coulomb}} \tag{94}$$

The idea is to multiply the central potential by a constant factor  $f$  only for the last neutron configuration:

$$V_{\text{central}}(r) = f V_{HF}(r), \begin{cases} f \neq 1 & \text{for last neutron configuration} \\ f = 1 & \text{otherwise} \end{cases} \tag{95}$$

A	$J^\pi$	$S_n$ (MeV)	$S_{2n}$ (MeV)
${}^6\text{He}$	$0^+$	1.87	0.97
${}^8\text{He}$	$0^+$	2.58	2.13
${}^9\text{Li}$	$\frac{3}{2}^-$	4.06	6.10
${}^{10}\text{Li}$	$(2^-)$	$-0.5 \pm 0.3$	$3.6 \pm 0.3$
${}^{11}\text{Li}$	$\frac{3}{2}^-$	$0.82 \pm 0.30$	$0.33 \pm 0.09$
${}^9\text{Be}$	$\frac{3}{2}^-$	1.67	20.56
${}^{10}\text{Be}$	$0^+$	6.81	8.48
${}^{11}\text{Be}$	$\frac{1}{2}^+$	0.51	7.32
${}^{12}\text{Be}$	$0^+$	3.17	3.67
${}^{13}\text{Be}$	$(\frac{1}{2}^-)$	$-1.8 \pm 0.5$	1.37
${}^{14}\text{Be}$	$0^+$	$2.0 \pm 0.5$	$0.2 \pm 0.3$
${}^{15}\text{B}$	$\frac{3}{2}^-$	2.77	3.74
${}^{16}\text{B}$	$(0^-)$	$-0.6 \pm 0.5$	$2.2 \pm 0.5$
${}^{17}\text{B}$	$(\frac{3}{2}^-)$	$1.7 \pm 0.5$	$1.1 \pm 0.7$

Table 3.3 - Nuclei with negative separation energies are unstable against neutron decay. Data are from Refs. [15, 16].

Thus, the last neutron configuration (last orbits) is treated differently from the other orbits in the H-F potential in order to reproduce the neutron separation energy of the neutron-rich nucleus. This model was successful to explain most features of the light-neutron rich nuclei as e.g., the quantities given in Table 3.3 [19, 20]. It can also explain the magnitude of the nuclear sizes, as shown in Table 3.1. In order to obtain the nuclear sizes, the rms radii of the occupied nucleon orbits are multiplied by the shell model occupation probabilities, which are also obtained in the calculations. The column indicated by  $j_{\text{halo}}$  in Table 3.3 displays the most probably occupied orbits. The final radius is obtained by adding the core radius, and is given in the rows indicated by SM.

To understand these results we show in Figure 8 the (a) core and orbital densities, as well as the (b) shell model densities [core density and orbital density  $\times$  occupation probability] for  ${}^{11}\text{Be}$ . The core density is calculated by the original HF potential. It shows a reasonable agreement with the experimental data. Due to the centrifugal barrier, the orbits with lower angular momenta have a longer tail and larger rms radii for the same separation energy. The single-particle orbits with lower angular momenta  $\ell \leq 1$  are very likely to be halo configurations, while the orbits with higher  $\ell$  are not. Similar results are obtained for  ${}^{11}\text{Li}$  [20].

A	$j_{\text{halo}}$	$\sqrt{\langle r^2 \rangle}_{\text{cal}}$ (fm)	$\sqrt{\langle r^2 \rangle}_{\text{exp}}$ (fm)
${}^9\text{Li}$ (core)		2.45	$2.41 \pm 0.02$
${}^{11}\text{Li}$	$1p_{1/2}$	5.36	
	$2s_{1/2}$	7.61	
SM		3.26	$3.16 \pm 0.11$
${}^{10}\text{Be}$ (core)		2.39	$2.46 \pm 0.03$
${}^{11}\text{Be}$	$2s_{1/2}$	6.49	
	$1p_{1/2}$	5.96	
	$1d_{5/2}$	3.79	
SM		2.90	$2.86 \pm 0.04$
${}^{15}\text{B}$ (core)		2.70	$2.83 \pm 0.25$
${}^{17}\text{B}$	$2s_{1/2}$	5.62	
	$1d_{5/2}$	3.95	

Table 3.4 - The second column gives the spins of the most probable occupied orbits in the nuclear halo of several nuclei. The third column is the result of Hartree-Fock calculations for the rms radii associated with these orbits, and the last column gives the rms radii of the matter distribution of these nuclei.

The success of the model let us conclude that the outer neutrons and the core have to be treated differently. That is, a simple mean field approach (as a traditional HF calculation) is likely to fail.

Of course, the factor  $f$  in Eq. 95 is arbitrary ( $f = 0.82$  for the last neutrons in  ${}^{11}\text{Li}$  [19]) and deserves a satisfactory explanation. It was claimed (e.g., [21]) that this problem can be remedied by using a relativistic mean field theory (RMF) instead of the usual (non-relativistic) H-F calculation. A sketch of the RMF-theory is given in Supplement D. An example of application of these calculations to describe the rms radii of  ${}^6\text{He}$  and  ${}^8\text{He}$  is given below following Ref. [22].

The “experimental” matter densities of these nuclei were extracted from  $\sigma_I$  by using Eqs. 2 and 3, with densities chosen to reproduce the experimental data. For light nuclei the harmonic oscillator density distribution (see Supplement A) gives a good approximation. But, in the same spirit of the HF calculations shown in Figure 8(a and b), different size parameters were given for the  $1s$  and  $1p$  orbital. The following density is obtained

$$\rho(r) = \frac{2}{\pi^{2/3}} \left\{ \frac{1}{a^3} e^{-r^2/a^2} + \frac{1}{b^3} \frac{N-2}{3} \left(\frac{r}{b}\right)^2 e^{-r^2/b^2} \right\} \quad (96)$$

The size parameters  $a$  and  $b$  are given in Table 3.5. Also shown are the rms radii for neutrons, protons and nucleons.  $\Delta R^{\text{rms}} = \Delta R_n^{\text{rms}} - R_p^{\text{rms}}$ .

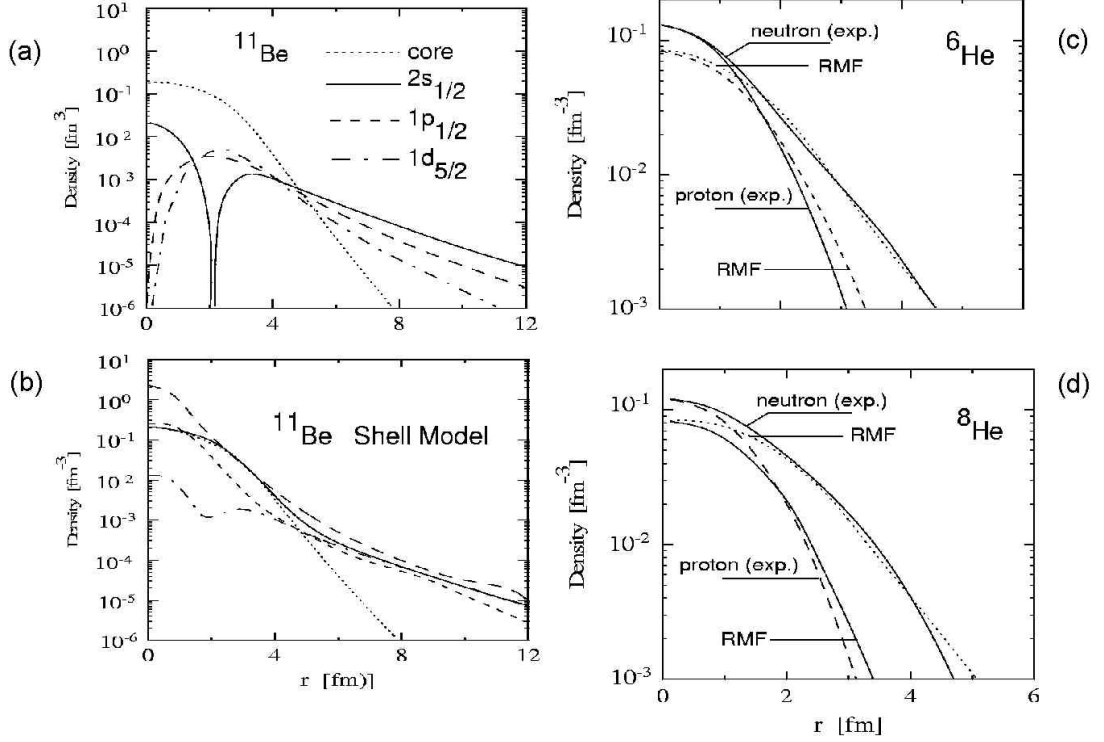


Figure 8 (a and b) Core and orbital densities (upper figure), as well as the shell model densities (lower figures). The core and orbital densities are multiplied by the occupation probabilities. The figures are from ref. [20]. (c and d) Relativistic Mean Field (RMF) calculations for the ground state densities of  $^6\text{He}$  and  $^8\text{He}$  (solid lines).

	Fitted par. <sup>a)</sup>		RMS radius (fm)			$\Delta R^{\text{rms}}$ (fm)
	a (fm)	b (fm)	$R_n$	$R_p$	$R_m$	
$^4\text{He}$	1.53	—	$1.63 \pm 0.03$	$1.63 \pm 0.03$	$1.63 \pm 0.03$	0
$^6\text{He}$	1.53	2.24	$2.59 \pm 0.04$	$1.72 \pm 0.04$	$2.33 \pm 0.04$	$0.87 \pm 0.06$
$^8\text{He}$	1.53	2.06	$2.69 \pm 0.04$	$1.76 \pm 0.03$	$2.49 \pm 0.04$	$0.93 \pm 0.06$

Table 3.5 - Parameters used in Eq. 96 to fit the radii of Helium isotopes.

A RMF calculation with the same parameters as those described in Supplement C was done [22] for the matter density distribution. As shown in Fig. 8(c and d) the agreement, with the “experimental” distributions is reasonable.

Since the number of neutrons in the outer orbits in  $^8\text{He}$  is large (4) but  $\Delta R^{\text{rms}}$  (see Table 3.5) is not much larger than that for  $^6\text{He}$ , the term “skin” nucleus was coined for  $^8\text{He}$  [22]. Neutron skins appear in many nuclei away from the stability line (close to the *drip line*). While a considerable number of neutrons can be included in a neutron skin, a neutron halo is expected to include only a few neutrons in the last orbital.

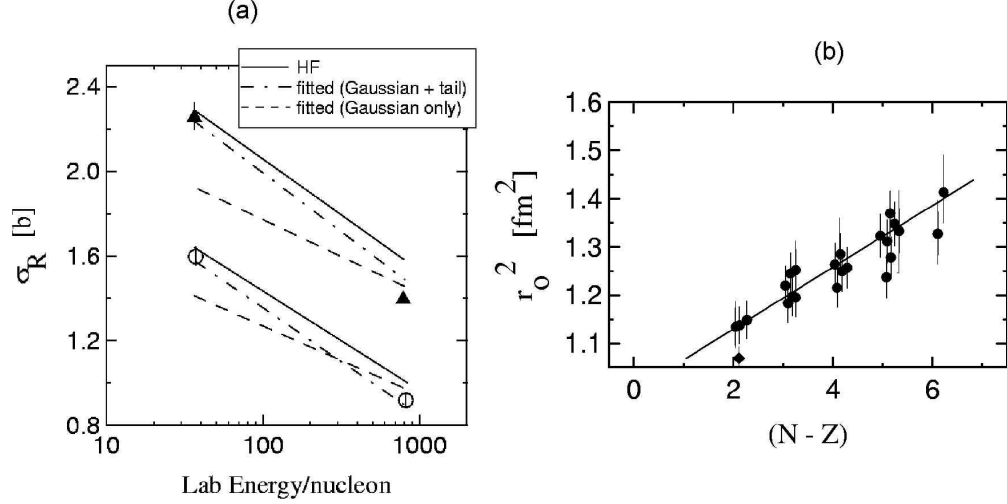


Figure 9 (a) Reaction cross section for  $^{11}\text{Be}$  with Al (upper points) and C (lower points) targets at two different energies, 33 MeV/nucleon and 790 MeV/nucleon. Hartree-Fock calculations and phenomenological Gaussian densities are also shown and are compared with the experiments. (b) Radius parameter used to fit the experimental reaction cross section, as a function of the neutron excess in several nuclei.

The fact emerging from the experiments is that the long tail of the matter distribution in some light neutron-rich nuclei is due to the small binding of the last neutrons. The contribution from the nucleons in the core and in the valence orbitals to the total matter distribution yield different distribution shapes. This fact is well displayed in figure 9(a) where a phenomenological density for  $^{11}\text{Be}$  was used to describe its reaction cross section with Al and C targets at two different energies, 33 MeV/nucleon and 790 MeV/nucleon, respectively. The  $^{11}\text{Be}$  was described as a  $^{10}\text{Be}$ -core + a valence neutron. The density distribution of  $^{10}\text{Be}$  was assumed to be a Gaussian which describes very well the matter distribution of light stable nuclei (see Figure 3). The wavefunction of a nucleon with separation energy  $\epsilon$  has a tail of the form  $e^{-\eta r/r}$  where  $\hbar^2\eta^2 = 2\mu\epsilon$  and  $\mu$  is the reduced mass. Thus, the valence neutron contributes with a density which is proportional to the square of this distribution. The summed distribution was used in Eqs. 2 and 3, and the reaction cross section was compared with the experiment. One sees that a single Gaussian distribution is unable to describe both set of data simultaneously. But a Gaussian plus a distribution obtained from a Yukawa function does it quite well. Also shown is the result of a calculation (solid line) using the modified HF (MHF) method described by Eqs. 93, 94, 95.

We conclude that the matter distribution in  $^{11}\text{Li}$  and  $^{11}\text{Be}$  is much like what one sees in the figure 10. The calculations support the idea that the nuclei possess a “halo” generated by the loosely-bound neutrons in the last orbit.

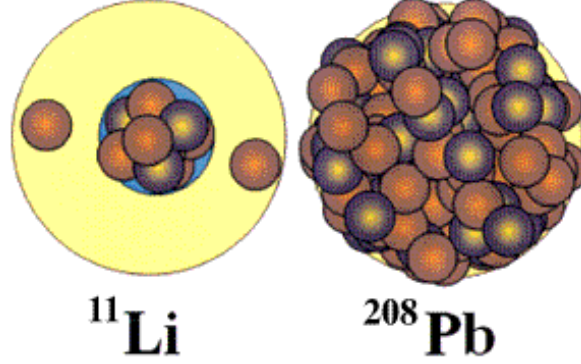


Figure 10 Left side: Light exotic nucleus, with a halo formed by loosely-bound nucleons and a tight core ( $^{11}\text{Li}$ ). Right side: a normal heavy nucleus ( $^{208}\text{Pb}$ ).

## 6 Intermediate energy experiments

$\sigma_I$  does not really represent the reaction cross section  $\sigma_R$ . For loosely-bound nuclei the two definitions converge since any excitation of these nuclei are likely to lead to their disruption. Thus,  $\sigma_I \sim \sigma_R$  for  $E_{\text{lab}} \sim 500$  MeV/nucleon, or greater, with  $\sigma_I$  defined as in Eq. 1.

In reactions at lower energies the Coulomb repulsion between the nuclei play an important role. The reaction cross section in intermediate energy experiments is given by

$$\sigma_R = \pi R^2, \quad (97)$$

where  $R$  is the reaction radius of the two nuclei. For high energies  $R \simeq R_1 + R_2$ , where  $R_i$  is the matter radius of a sharp nuclear density for the nucleus  $i$ . In collisions at intermediate energies the nuclei are displaced due to Coulomb recoil when they are at the distance of closest approach. Thus situations for which the impact parameter  $b < R_1 + R_2$  will also contribute to the interaction cross section.

The recoil due to the Coulomb force implies that, for a collision with impact parameter  $b$ , the relative distance the nuclei at their closest approach is given by

$$d = b + \frac{Z_1 Z_2 e^2}{\mu v^2} = b + \frac{Z_1 Z_2 e^2}{2E_{\text{cm}}} \quad (98)$$

where  $E_{\text{cm}}$  is the center of mass energy, and  $\mu = \frac{m_1 m_2}{m_1 + m_2}$ , the reduced mass of the system.

Correcting for the recoil, the interaction radius to be used in 97 should be

$$R \simeq R_0 - \frac{Z_1 Z_2 e^2}{2E_{\text{cm}}} = R_0 \left( 1 - \frac{B}{2E_{\text{cm}}} \right), \quad (99)$$

where

$$B = \frac{Z_1 Z_2 e^2}{R_0} \quad (100)$$

is called the barrier energy.

Thus, 97 becomes

$$\sigma \cong \pi R_0^2 \left( 1 - \frac{B}{E_{\text{cm}}} \right) \quad (101)$$

To fit the reaction cross sections the following parametrization for  $R_0$  was found useful [23]:

$$R_0 = r_0 \left( A_1^{1/3} + A_2^{1/3} + b \frac{A_1^{1/3} A_2^{1/3}}{A_1^{1/3} + A_2^{1/3}} - c + d \right) \quad (102)$$

with  $r_0 = 1.1$  fm and  $b = 1.9$ . The first two terms correspond to the sum of the nuclear radii for sharp nuclear distributions. The third term (proportional to  $b$ ) accounts for the volume overlap of the two colliding nuclei. The parameter  $c$  is energy dependent and takes care of the increasing surface transparency as the projectile energy increases. It can be parametrized as

$$c = 0.14 + 0.015 \frac{E_{\text{cm}}}{A} \quad (103)$$

for energies  $E_{\text{cm}}/A$  around 50 MeV/nucleon. At relativistic energies ( $\gtrsim 500$  MeV/A) it reaches the asymptotic value of  $c = 1.9$ . The factor  $d = 5(N_2 - Z_2)Z_1/(A_1 A_2)$  accounts for the neutron excess in the target (nucleus 2) and is important only for the heaviest targets. It can be neglected for light or medium-light ones [23].

In some experiments [24, 25] the total reaction cross section for neutron-rich light nuclei was measured for several targets at intermediate bombarding energies ( $E_{\text{cm}}/A \sim 50$  MeV/nucleon). The reaction cross sections were determined by measuring  $\gamma$ -rays with a  $4\pi$ -detector. The emission of  $\gamma$ -rays determines reliable total reaction cross sections over a wide range of energies, projectiles and targets <sup>‡</sup>.

A deviation from the parametrization 102 would indicate an abnormal matter distribution. In Ref. [24] this deviation was stated in terms of the value of  $r_0$  needed to reproduce the  $\sigma_r$ 's. In principle  $r_0$  should be a constant. Results from Ref. [24] are shown in Fig. 9(b) where  $r_0^2$  is plotted as a function of the neutron excess for various atomic numbers. One sees that  $r_0^2$  has a strong dependence on  $(N - Z)$  for several isotopes. Such a strong dependence is again an evidence that a long-range nuclear-matter distribution is responsible for the effect. The data show a single trend for all atomic numbers and it is not likely that such a structure effect will show up independently of the proton number. This long-range tail is due to an increase of the diffuseness, or a neutron halo (as shown pictorially in Figure 1.10).

The advantage of the  $4\pi - \gamma$  measurements of Fig. 9(b) over the high energy experiments is that the evidence of an abnormally large matter distribution is obtained by a model independent extraction of the matter radii, while in the high energy experiments an eikonal model with phenomenological matter distributions was needed in order to extract the *rms* radii of the neutron-rich nuclei.

<sup>‡</sup>The basic assumption is that a nuclear reaction is characterized by the emission of at least one  $\gamma$ -ray.

Theoretical predictions for the density distribution of exotic neutron-rich nuclei are not straight forward. In fact, theoretical calculations only came after the fact, i.e., after the measurements were done.

## 7 Reaction model with few-body wavefunctions

The approach presented in the previous Sections neglect the correlations between the projectile (and target) constituents, each projectile nucleon being assumed to carry the same single particle density [26]. For weakly bound systems such as halo nuclei, however, the intrinsic few-body nature or granularity of the projectiles imply strong spatial correlations between the valence nucleons and the more localized core. At incident energies of order 800 MeV/nucleon one must also consider the relevant time scales for a significant motion of these valence particles inside the projectile and that for the passage of the same particle through the target interaction region. In breakup studies narrow momentum widths are associated with these valence particles which have characteristic kinetic energies of order 10–40 MeV within the projectile. For this reason some reaction models [27, 28] make a sudden approximation, freezing the position coordinates of the few-body projectile constituents during the interaction. Physical observables are then obtained by suitably averaging the resulting position dependent reaction amplitudes over the relevant position probability distributions of these constituents. This important idea was recognized by Al-Khalili and J.A. Tostevin [29] and is the subject of this Section (see also Supplement D).

Consider for example  $^{11}\text{Li}$  as a pair of neutrons bound to a  $^9\text{Li}$  core (see Figure 11). For an impact parameter  $b$  of the  $^{11}\text{Li}$  center of mass such that the projectile static density (shaded circle) overlaps the target, many spatial configurations of the constituent bodies will not overlap the target. The expectation is that the valence nucleon (large  $b$ ) contribution to the reaction cross section will be reduced or, alternatively, that the collision will appear more transparent than otherwise expected. Nishioka and Johnson [30] investigated related sudden approximation effects on light-ion composite projectile (d, t,  $^3\text{He}$  and  $\alpha$ ) cross sections in the energy range  $100 \leq E \leq 350$  MeV/nucleon. The effects were very significant for the extended deuteron but small for the  $\alpha$  particle.

According to Eq. ??, the reaction cross section for projectile  $P$  is

$$\sigma_R(P) = 2\pi \int_0^\infty db b [1 - T_P(b)], \quad (104)$$

where  $T_P(b)$ , the squared modulus of the Glauber  $S$ -matrix, is the transparency function of the collision at impact parameter  $b$ . In the optical limit of the Glauber theory the transparency function is given by

$$T_P^{\text{OL}}(b) = \exp \left[ -\sigma_{\text{NN}} \int d^2\mathbf{x} \rho_P^{(z)}(|\mathbf{x}|) \rho_T^{(z)}(|\mathbf{b} - \mathbf{x}|) \right], \quad (105)$$

where

$$\rho_i^{(z)}(b) = \int_{-\infty}^{\infty} dz \rho_i(\sqrt{b^2 + z^2})$$

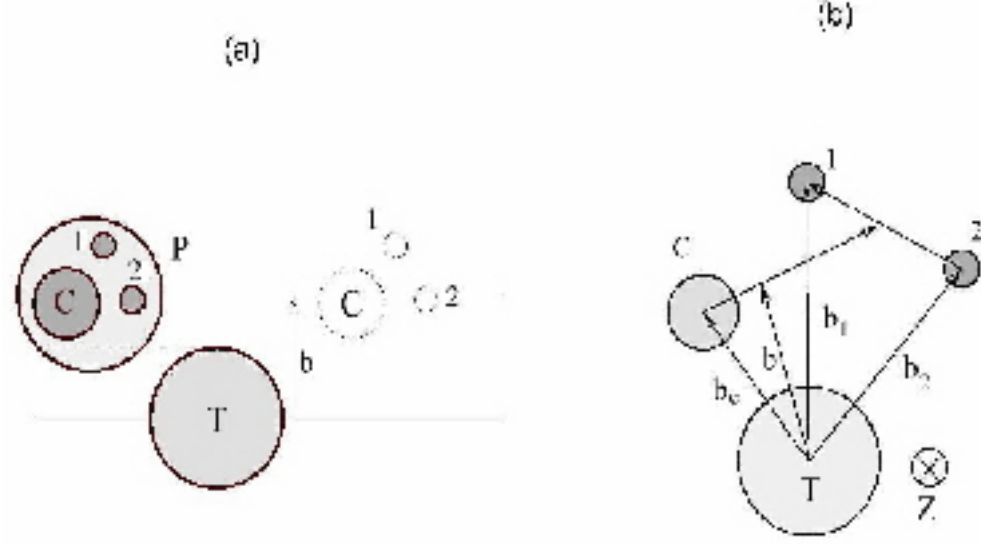


Figure 11 (a) Schematic representation of the static density (shaded circle) and few-body adiabatic (frozen coordinate) treatments of the three-body projectile (P)-target (T) collision at impact parameter  $b$ . In the spatial configuration drawn the few-body projectile does not overlap the target. (b) Definition of position coordinates, in the plane perpendicular to the beam direction, in the case of a three-body (two valence nucleon+core) projectile.

are the  $z$ -integrated densities or thickness functions. Here only the projectile ground state density enters the calculation and few-body correlations, the granular nature of the projectile, does not enter explicitly.

For halo nuclei it is more appropriate to separate the core and the valence nucleon contributions. In the few-body sudden limit, the transparency function is [31],

$$T_P^{\text{SA}}(b) = |\langle \Phi_0^n | S_C(b_C) S_v(b_v) | \Phi_0^n \rangle|^2 ,$$

where  $|\Phi_0^n\rangle$  is the wavefunction for the  $n$ -constituent bodies in the projectile ground state, the bra-ket denoting integration over these internal coordinates. For a two-body (one valence nucleon+core) projectile the core-target and valence nucleon-target  $S$ -matrices, in the optical limit, are

$$S_C(b_C) = [T_C^{\text{SA}}(b_C)]^{1/2} , \quad S_v(b_v) \equiv S_1(b_1) = [T_N^{\text{SA}}(b_1)]^{1/2} ,$$

with  $b_C$  the impact parameter of the core and  $T_N^{\text{SA}}$  the analogue of Eq. (105) for the nucleon. For a three-body (two valence nucleon+core) system, then of course

$$S_v(b_v) \equiv S_1(b_1) S_2(b_2), \quad (106)$$

where the coordinates, in the plane perpendicular to the beam direction, are shown in Figure 11. Eqs. (104) through (106) were calculated exactly in the following for

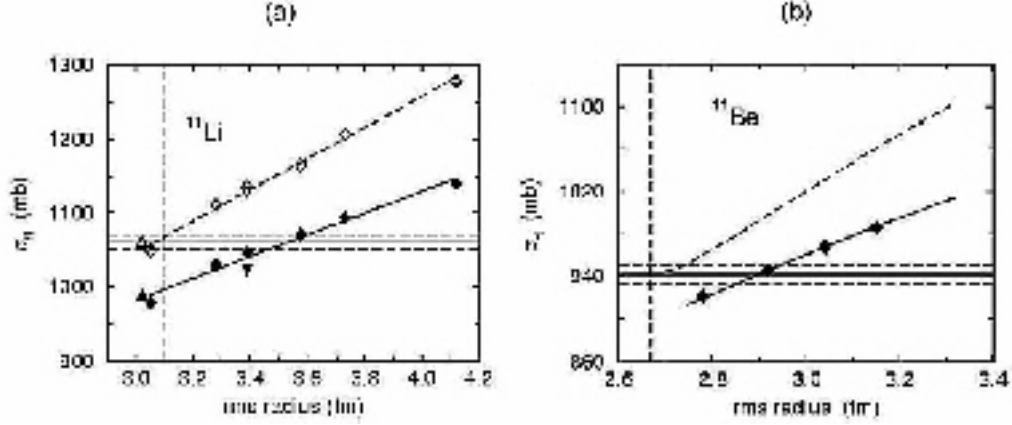


Figure 12 (a) Calculated static density and few-body adiabatic reaction cross sections at 800 MeV/nucleon incident energy as a function of projectile rms matter radius, for a  $^{12}\text{C}$  target for  $^{11}\text{Li}$  projectiles. (b) Same as in (a), but for  $^{11}\text{Be}$ .

realistic two- and three-body wavefunctions  $|\Phi_0^n\rangle$ . The explicit forms of the three-body wavefunction for  $^{11}\text{Li}$  are given in [28].

The formalism above was used [29] to calculate reaction cross sections in the static density and sudden limits for the one- and two-neutron halo nuclei  $^{11}\text{Be}$  and  $^{11}\text{Li}$ , and the one-proton halo nucleus candidate  $^8\text{B}$ , all on a  $^{12}\text{C}$  target at 800 MeV/nucleon. A Gaussian matter distribution is assumed for  $^{12}\text{C}$  in all cases with rms matter radius  $\langle r^2 \rangle_{12}^{1/2} = 2.32$  fm. With these inputs, and assuming Gaussian matter distributions for the core nuclei with radii  $\langle r^2 \rangle_9^{1/2} = 2.30$  fm,  $\langle r^2 \rangle_{10}^{1/2} = 2.28$  fm and  $\langle r^2 \rangle_7^{1/2} = 2.31$  fm, the calculated reaction cross sections for the core-target subsystems are  $\sigma_R(^9\text{Li}) = 796$  ( $796 \pm 6$ ) mb,  $\sigma_R(^{10}\text{Be}) = 813$  ( $813 \pm 10$ ) mb and  $\sigma_R(^7\text{Be}) = 738$  ( $738 \pm 9$ ) mb. The empirical values, in parentheses, are taken from [32]. The deduced core radii agree with those of [2] within error bars. The calculated nucleon- $^{12}\text{C}$  cross section at 800 MeV is  $\sigma_R(N) = 231$  mb which also agrees with experiment [33] within quoted errors. Thus each projectile constituent-target input to the few-body calculations, the  $S_C$  and  $S_v$ , is consistent with independent empirical data for that binary system.

Figure 12(a) shows the results of static density and sudden approximation calculations for the  $^{11}\text{Li}+^{12}\text{C}$  system for a number of theoretical three-body wavefunctions of  $^{11}\text{Li}$ . The calculated cross sections versus the matter rms radius calculated from the wavefunction models is shown. The horizontal band shows the experimental interaction cross section datum  $\sigma(^{11}\text{Li}) = 1060 \pm 10$  mb [34] and the vertical dashed line the previously quoted matter radius  $\langle r^2 \rangle_{11}^{1/2} = 3.10 \pm 0.17$  fm [2].

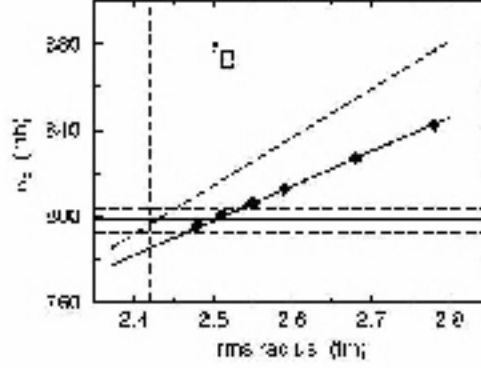
The (upper) open symbols are the results of the static density model and the (lower) full symbols those of the sudden approximation calculations for each wavefunction model. The reduction in the calculated cross sections, or increased transparency of the projectile in the latter case, is immediately evident. From left to right

the diamond symbols correspond to the P0 through P4 intruder  $s$ -wave (Faddeev) model wavefunctions of Thompson and Zhukov [35], with increasing rms radius. The extreme right hand point is a continuation of these model wavefunctions (P5) with a  $1s$ -state scattering length of  $-44$  fm and 80%  $(1s_{1/2})^2$  probability. The upright and inverted triangles are calculations using the L6A pairing model wavefunction [36], which in the static density picture fits the published radial value, and the weak binding potential  $0s$ -wave intruder wavefunction (G1 of [35]). The straight lines through these model points are to guide the eye.

The results of these calculations are indeed dramatic. Whereas static density calculations suggest a matter rms radius of order 3.1 fm, as reported previously, a correct treatment of the  $^{11}\text{Li}$  three-body character now suggests the halo is very much more extended and that  $\langle r^2 \rangle_{11}^{1/2} = 3.55 \pm 0.10$  fm, firmly in the middle of the range of values generated by intruder state models which successfully reproduce empirical breakup momentum distributions [35].

Figure 12(b) shows the results of similar calculations but for the one-neutron halo system  $^{11}\text{Be}$ . Again the horizontal band shows the experimental cross section datum  $\sigma(^{11}\text{Be}) = 942 \pm 8$  mb [32] and the vertical dashed line the previously reported rms matter radius  $\langle r^2 \rangle_{11}^{1/2} = 2.71 \pm 0.05$  fm [2]. The results are qualitatively very similar to those of the three-body  $^{11}\text{Li}$  case. The angled dashed line shows the static density calculations and the angled solid line and full symbols the sudden model results. In this case these lines connect a large number of calculations using simple two-body  $(1s_{1/2})$  cluster wavefunctions for  $^{11}\text{Be}$  using binding potentials with a range of geometries and with depth adjusted to reproduce the single neutron separation energy 0.503 MeV. The solid symbols are the results of sudden model calculations for  $^{11}\text{Be}$  wavefunctions [38] which include the effects of core ( $^{10}\text{Be}$ ) deformation and excitation. The wavefunction with rms radius 2.92 fm, whose calculated cross section lies within experimental error bars, best reproduces the excited state spectrum of  $^{11}\text{Be}$ . These wavefunctions generate cross sections which follow precisely the trend of the inert core calculations and suggest a revised matter rms radius of  $\langle r^2 \rangle_{11}^{1/2} = 2.90 \pm 0.05$  fm.

Finally, in Figure 13 we consider the one proton-halo nucleus candidate  $^8\text{B}$ . The previously reported value of  $\langle r^2 \rangle_8^{1/2} = 2.39 \pm 0.04$  fm [2] was very close to that for  $^7\text{Be}$ ,  $\langle r^2 \rangle_7^{1/2} = 2.33 \pm 0.02$  fm [2] suggesting, in spite of the very small proton separation energy (0.137 MeV) that the last proton had rather limited extension. The experimental cross section for  $^8\text{B}$  has been revised to  $\sigma(^8\text{B}) = 798 \pm 6$  mb and is shown by the horizontal band on the figure. Using the static density model and a Gaussian density, in the manner of [2], one obtains a revised static density estimate of  $\langle r^2 \rangle_8^{1/2} = 2.42 \pm 0.03$  fm, shown by the vertical dashed line. The angled dashed and solid lines are the results of static density and sudden model calculations for a large number of two-body  $(0p_{3/2})$  cluster wavefunctions for  $^8\text{B}$  based on Woods-Saxon potential geometries. The diamonds use wavefunctions based on the often used cosh form cluster model interaction [39] and lie on the same lines. Although the differences between the model calculations are smaller than in the neutron halo cases, they remain very significant and suggest the rms radius of  $^8\text{B}$  should be revised

Figure 13 Same as figure 12, but for  ${}^8\text{B}$ .

to  $\langle r^2 \rangle_8^{1/2} = 2.50 \pm 0.04$  fm, indicating quite significant extension of the last proton distribution beyond that of the core.

---

## Supplement D

---

### 8 Cluster aspect correction of $\sigma_R$

The expression for the total reaction cross-section using the eikonal form for the S-matrix, namely

$$\sigma_R = 2\pi \int b db (1 - |S|^2) \quad (107)$$

is valid for nuclei which are close-packed. For halo nuclei, one should consider  $S$  as an operator (depending on the relative coordinate of the two fragments forming the projectile) and thus take the ground state expectation value of  $S$ , viz.,

$$\sigma_R = 2\pi \int b db (1 - \langle \phi_0 | \hat{S} | \phi_0 \rangle^2) \quad (108)$$

Using the eikonal form for  $S$ , namely ( $\alpha$  stands for other variables of the optical potential)

$$\hat{S}(\chi) = \exp \left[ -\frac{i}{\hbar v} \int_{-\infty}^{\infty} V(\sqrt{b^2 + z^2}; \alpha) dz \right] = \exp[-i\chi(b, \alpha)]$$

one has for purely absorptive potentials

$$\langle \phi(\alpha) | e^{-i\chi(b, \alpha)} | \phi(\alpha) \rangle \geq e^{-i\langle \chi(b, \alpha) | \phi \rangle}$$

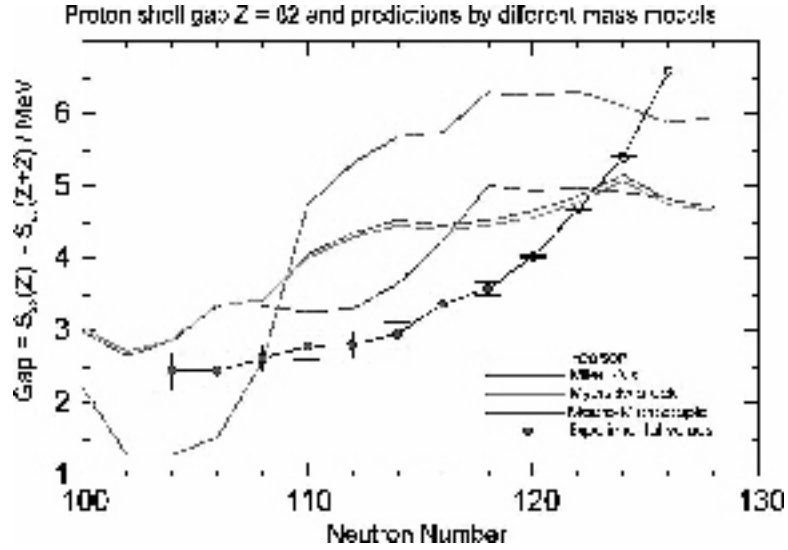


Figure 14 Experimental proton shell gap (dots with error bars) for proton deficient the lead isotopes compared to theoretical predictions.

Clearly,  $\sigma_R$ , calculated with the correct form  $\langle \phi | e^{-i\chi} | \phi \rangle$  is smaller than that calculated with the usual eikonal form of the previous discussion. Though proving the above inequality for general complex  $V$ , the numerical calculations presented in the last Section [29], have shown that the trend is similar. To reproduce the experimental  $\sigma_R$ , with a smaller calculated  $\sigma_R$  one requires a larger radius. The conclusion one reaches is that the radii of halo nuclei are  $> 10\%$  larger than previously believed (and shown in Table 3.4).

## 9 Mass measurements of exotic nuclei

A powerful tool for large-scale mass measurements are heavy-ion storage and cooler rings. As an advantage in comparison to ion traps, storage rings can accumulate in-flight separated atomic nuclei at their full energy and with large phase space, e.g., many masses can be measured simultaneously.

The nuclides of interest are produced by projectile fragmentation. The mass-over-charge ratios are obtained from the Fourier-transformed noise signal of the coasting ions. This *Schottky-Mass-Spectroscopy*, is very precise and extremely sensitive. It permits the measurement even of single ions. In the first experiments 104 new masses of proton rich nuclides ranging from tellurium to plutonium [40] were obtained by direct mass measurement of the stored projectile fragments and by combining the known  $Q_\alpha$  values along the  $\alpha$  - decay chains of the trans-bismuth isotopes to masses at their endpoints, determined directly in the experiment.

As an example selected from the results, Fig. 14 shows the persistence of the lead shell in dependence from the neutron number. The lead shell gap decreases fast towards the proton rich side. This is not predicted by the displayed models

[41, 42, 43].

## 10 References

1. I. Tanihata et al., Phys. Rev. Lett. **55** (1985) 2676.
2. I. Tanihata, T. Kobayashi, O. Yamakawa, S. Shimoura, K. Ekuni, K. Sugimoto, N. Takahashi, T. Shimoda and H. Sato, Phys. Lett. **B206** (1988) 592.
3. *Handbook of Mathematical Functions*, edited by M. Abramowitz and I. Stegun (U.S.GPO, Bureau of Standards, Washington, DC, 1964).
4. P.J. Karol, Phys. Rev. **C11** (1975) 1203.
5. M.G. Mayer and J.H. Jensen, *Elementary Theory of Nuclear Shell Structure*, John Wiley and Sons, New York (1955).
6. T. Kobayashi, Nucl. Phys. **A538** (1992) 343c.
7. I. Tanihata, on “*Treatise on Heavy-Ion Science*”, Vol. 8, Ed. by D. Allan Bromley, (Plenum Publ., 1989).
8. T.H.R. Skyrme, Proc. Phys. Soc. (London) **A70** (1957) 433.
9. T.H.R. Skyrme, Nucl. Phys. **9** (1959) 615.
10. D. Vautherin and D.M. Brink, Phys. Rev. **C5** (1972) 626.
11. S. Koonin et al., eds, “*Computational Nuclear Physics*”, Springer, NY, 1989.
12. H. Goldstein, “*Classical Mechanics*”, Addison Wesley, Massachusetts, 1980.
13. B.D. Serot and J.D. Walecka, Adv. Nucl. Phys. **16** (1986) 1.
14. C. Mahaux, P.F. Bortignon, R.A. Broglia and C.H. Dasso, Phys. Rep. **120** (1985) 1.
15. K.H. Wilcox et al., Phys. Lett. **B59** (1975) 142.
16. A.I. Amelin et al., J. Nucl. Phys. **42** (1990) 782.
17. V. Bernard and Nguyen van Giai, Nucl. Phys. **A348** (1980) 75.
18. Z.Y. Ma and J. Wambach, Nucl. Phys. **A402** (1983) 275.
19. G.P. Bertsch, B.A. Brown and H. Sagawa, Phys. Rev. **C39** (1989) 1154.
20. H. Sagawa, Phys. Lett. **B286** (1990) 7.
21. W. Koepf, Y.K. Gambhir, P. Ring and M.M. Sharma, Z. Phys. **A340** (1991) 119.
22. I. Tanihata et al., Phys. Lett. **B289** (1992) 261.
23. S. Kox et al., Phys. Rev. **C35** (1987) 1678.
24. W. Mittig et al., Phys. Rev. Lett. **59** (1987) 1889.
25. M.G. Saint-Laurent et al., Z. Phys. **A332** (1989) 457.
26. W. Czyz and L.C. Maximon, Ann. Phys. (N.Y.) **52** (1969) 59.
27. K. Yabana, Y. Ogawa and Y. Suzuki, Phys. Rev. **C45**, 2909 (1992); Nucl. Phys. **A539** (1992) 295.
28. J.S. Al-Khalili, I.J. Thompson and J.A. Tostevin, Nucl. Phys. **A581** (1995) 331.
29. J.S. Al-Khalili and J.A. Tostevin, Phys. Rev. Lett. **76** (1996) 3903.
30. H. Nishioka and R.C. Johnson, Phys. Rev. **C22** (1980) 2457; J. Phys. G: Nucl. Phys. **8** (1982) 39; these arguments have also been used in the previous papers: L.V. Chulkov, B.V. Danilin, V.D. Efros, A.A. Korshennikov and M.V. Zhukov, Europhys. Lett. **8** (1989) 245; N. Takigawa, M. Ueda, M. Kuratani and H. Sagawa, Phys. Lett. **B288**

- (1992) 244.
31. Y. Ogawa, K. Yabana and Y. Suzuki, Nucl. Phys. **A543** (1992) 722.
  32. I. Tanihata et al., Phys. Lett. **B160** (1985) 380.
  33. W. Bauhoff, Atomic Data and Nuclear Data Tables **35** (1986) 429.
  34. T. Kobayashi et al., Phys. Lett. **B232** (1989) 51.
  35. I.J. Thompson and M.V. Zhukov, Phys. Rev. **C49** (1994) 1904.
  36. J.M. Bang and I.J. Thompson, Phys. Lett. **B270** (1992) 201.
  37. L. Johannsen, A.S. Jensen and P.G. Hansen, Phys. Lett. **B244** (1990) 357.
  38. F.M. Nunes, I.J. Thompson and R.C. Johnson, Nucl. Phys. **A596** (1996) 171.
  39. B. Buck and A. Pilt, Nucl. Phys. **A280** (1977) 133.
  40. Th. Radon et al., Nucl. Phys. **A677** (2000) 75.
  41. P. Möller, J. R. Nix, W.D. Myers, and W.J. Swiatecki, At. Nuc. Dat. Tables **59** (1995) 185.
  42. W. D. Myers et al., Phys. Rev. **C583** (1998) 368.
  43. J. M. Pearsson et al., Nucl. Phys. **A528** (1991) 1; At. Nuc. Dat. Tables **61** (1995) 127.